

Article

OTFS-IM Modulation Based on Four-Dimensional Spherical Code in Air-to-Ground Communication

Peng Gu ^{1,†}, Lin Guo ^{1,†} , Shen Jin ², Guangzu Liu ^{1,*} and Jun Zou ^{1,*} 

¹ School of Electronic and Optical Engineering, Nanjing University of Science and Technology, Nanjing 210094, China; gupenghy@njjust.edu.cn (P.G.); lin_guo@njjust.edu.cn (L.G.)

² State Grid Jibei Information & Telecommunication Company, Beijing 100053, China; jin.shen@jibei.sgcc.com.cn

* Correspondence: liuguangzu@njjust.edu.cn (G.L.); jun_zou@njjust.edu.cn (J.Z.); Tel.: +86-137-7061-5557 (J.Z.)

† These authors contributed equally to this work and should be considered co-first authors.

Abstract: Unmanned aerial vehicles (UAVs) have been widely utilized for their various advantages. However, UAVs exhibit high mobility and energy storage restrictions in some applications, which can compromise the quality and reliability of communication links. This is a challenge that future aircraft and low-orbit aircraft will inevitably encounter. To effectively address the issue of dynamic Doppler spread in air-to-ground communication, this paper creatively introduces four-dimensional spherical code modulation into the orthogonal time–frequency space with an index modulation (OTFS-IM) system. The fundamental concept of the four-dimensional spherical code is elaborated in detail. Multiple resource symbols can be jointly used to increase the modulation dimension, thereby achieving a larger minimum Euclidean distance between constellation points. Furthermore, detailed analysis is conducted on the bit error rate (BER) and the peak-to-average-power ratio (PAPR) expressions of the proposed system to evaluate its performance and provide theoretical guidance. The proposed scheme not only adapts well to high-speed scenarios but also achieves better power consumption efficiency. The simulation results demonstrate that our proposed scheme outperforms conventional methods. Its robustness and generalization ability are also validated.

Keywords: orthogonal time–frequency space; index modulation; spherical code; maximum likelihood detection



Citation: Gu, P.; Guo, L.; Jin, S.;

Liu, G.; Zou, J. OTFS-IM Modulation

Based on Four-Dimensional Spherical

Code in Air-to-Ground

Communication. *Drones* **2023**, *7*, 631.

<https://doi.org/10.3390/drones7100631>

Academic Editors: Emmanouel

T. Michailidis and Petros Bithas

Received: 3 September 2023

Revised: 1 October 2023

Accepted: 9 October 2023

Published: 10 October 2023



Copyright: © 2023 by the authors.

Licensee MDPI, Basel, Switzerland.

This article is an open access article

distributed under the terms and

conditions of the Creative Commons

Attribution (CC BY) license ([https://creativecommons.org/licenses/by/](https://creativecommons.org/licenses/by/4.0/)

[https://creativecommons.org/licenses/by/](https://creativecommons.org/licenses/by/4.0/)

4.0/).

1. Introduction

With the continuous development of information technology, the space range of information service has expanded from well-developed terrestrial communication to air-to-ground (A2G) communication and satellite communication. Unmanned aerial vehicles (UAVs) have become a very attractive research topic in A2G communication and satellite communication owing to their various advantages, such as mobile flexibility, small size, and low cost [1–3]. UAVs can have significant influence in agriculture, aerial surveys, and public rescue, and can even be used as a satellite communication relay to expand coverage and ensure communication quality. The drone network has also been developed comprehensively, such as through a novel offset feedback fractionally spaced equalization architecture, the design of drone-aided IoT networking, and a high-mobility support system for NTN connectivity [4–6]. In terms of profit, a UAV can be used as a cost-effective air platform for A2G communications. However, one major feature of A2G communication is its dynamic mobility. For example, in common UAV scenarios, speeds of 161 km/h may be reached. In certain scenarios, such as when using military UAVs and future aircraft, the flight speed can reach even more than 500 km/h, at which speeds they experience large path loss and serious Doppler spread, which may hinder the quality of the A2G link [7,8]. Therefore, it is very important to study robust A2G wireless links for high-speed A2G communication.

OFDM technology is widely used in terrestrial communication, such as 4G, because of the advantage of orthogonal subcarriers. However, with the increase in Doppler spread, orthogonality is no longer maintained [9]. Orthogonal time–frequency space (OTFS) modulation, a novel 2D modulation in the delay–Doppler (DD) domain, has been proposed to solve this problem; this allows the time and frequency diversity to be fully exploited by the 2D convolution between the modulation symbols and the effective channel in the DD domain [10]. The effective channel in the DD domain achieves near-constant channel gain, which is quite different from time-varying channels in the time–frequency (TF) domain. At the same time, the channel is sparse because there are limited reflectors in the propagation path, which is beneficial to the design of the receiver [11,12].

According to the characteristics of the channel, many studies on signal detection have been carried out, such as on LMMSE, MP, MRC, and Bayes schemes [13–16]. In practical signal detection, the correct channel state information is also indispensable. Some effective approaches have also been developed, such as the classical threshold-based method, orthogonal matching tracking (OMP), sparse Bayes, and our previous work on a DNN-based scheme [17–20]. Additionally, some novel structure designs for OTFS have been proposed. Explicitly, in order to convey additional information in high-mobility scenarios, a new OTFS scheme with index modulation (OTFS-IM) is proposed in [21], which explores a new dimension. Compared with the conventional OTFS modulation, OTFS-IM modulation can convey additional index information by combining active and silent DD domain symbols to improve spectral efficiency. Moreover, the transmitted data in DD domain are sparser, which effectively reduces the interference and also leads to a significant gain in bit error rate (BER) performance. The authors in [22] explored the potential of OTFS-IM modulation and proposed an OTFS-IM with dual-mode modulation (OTFS-DM-IM), where the symbols in the DD domain are modulated by two constellation matrices to transmit more additional index bits, thus achieving a higher transmission rate. To increase the spectral efficiency of the existing OTFS-IM schemes, there is a new transmission scheme called OTFS-I/Q-IM [23]. By extending the grid index of OTFS systems to in-phase and quadrature dimensions, this new scheme has two index dimensions and L -ary PAM constellation symbols to transmit information. However, most of the existing methods obtain a better detection performance by increasing the index dimensions, which increases the number of modulation steps and makes the transmitter design more complex.

Another major feature of A2G communication in the UAV scenario is the limited energy of the UAV. Due to its small size, there are restrictions on payload and energy storage, which prevent it from performing remote operations over a long time [24]. Therefore, low-power communication research is still of great significance for an A2G network. Currently, most of the work on OTFS and OTFS-IM systems is based on two-dimensional modulation, such as quadrature amplitude modulation (QAM). In fact, it is possible to utilize multiple resource symbols jointly to increase the modulation dimension. For example, we can achieve four dimensions by combining two symbols together. According to the classical detection theory, a higher modulation dimension could have a larger minimum Euclidean distance between constellation points if it is elegantly designed, which confers better anti-interference and detection performance [25].

Given that the traditional OTFS-IM modulation could be improved and there are resource constraints on the UAV communication, it is critically important to design an optimal and practical OTFS-IM system for A2G communication. To this end, this paper creatively introduces four-dimensional spherical code into the OTFS-IM system, denoted as OTFS-IM4, where the spherical code is similar to the sphere packing problem [26]. Correspondingly, the conventional two-dimensional modulation is denoted as OTFS-IM2. The main contributions of this paper are as follows:

- To enhance the endurance of UAVs, an OTFS-IM system based on four-dimensional spherical code is proposed in this paper, which allows the OTFS-IM system to have good signal detection performance under low signal-to-noise ratio. The design and implementation of this system are elaborately described in the paper;

- In addition, this paper analyzes the proposed system, both analytically and numerically, to derive the approximate value of the bit error rate (BER) and the upper bound of the peak-to-average-power ratio (PAPR), which has general guiding significance.

The rest of the paper is organized as follows: Section 2 introduces the basic model of the OTFS-IM system with the high-dimensional spherical code. Section 3 analyzes the performance of BER and PAPR in our proposed scheme. Section 4 verifies the effectiveness of the high-dimensional modulation and the practical significance of the theoretical analysis in Section 3. Finally, Section 5 concludes the paper.

2. System Model

We consider an OTFS-IM frame with M subcarriers and N symbols. The subcarrier spacing and symbol duration are denoted as Δf and T , respectively. Therefore, an OTFS-IM frame with duration NT and bandwidth $M\Delta f$ could be treated as an $M \times N$ grid in the DD domain. The block diagram of the OTFS-IM system with four-dimensional spherical code modulation is shown in Figure 1. It is assumed that there are n symbols and k active symbols in a sub-block, where “symbols” here represents bins in the DD grid. Then, an OTFS-IM4 frame can be divided into $g = MN/n$ groups. The transmitted bit set \mathbf{u} is evenly divided into g groups, where each sub-block transmits $p = p_1 + p_2$ bits. Specifically, the p_1 bits and p_2 bits are used for index selection and constellation mapping, respectively. Since all OTFS-IM4 sub-blocks are independent of each other, the β -th sub-block is taken as an example for description.

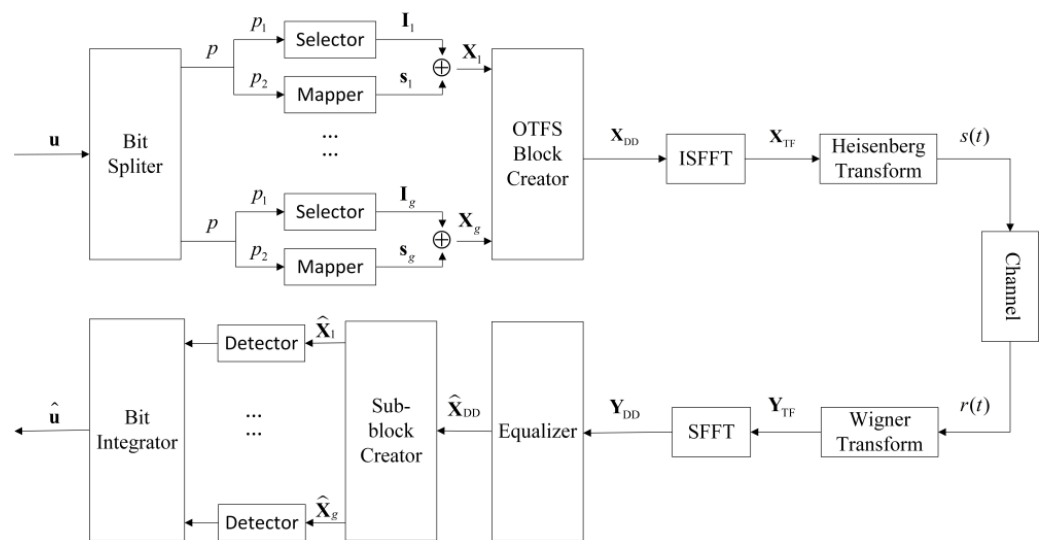


Figure 1. Block diagram of OTFS-IM4 system.

As mentioned before, increasing the dimensions enables a larger Euclidean distance between constellation points when the design is elegant. We mainly consider four-dimensional spherical code modulation as constellation mapping in this paper. To begin with, Ω_L represents the surface of the unit sphere in L -dimensional space:

$$\Omega_L = \left\{ \mathbf{c} = \{c_1, c_2, \dots, c_L\} \in \mathbb{R}^L \mid \sum_{l=1}^L c_l^2 = 1 \right\} \tag{1}$$

where \mathbf{c} is a point on Ω_L , and c_l is the amplitude of the l -th dimension. Taking M_c points of the surface as the modulation constellation alphabet \mathcal{A} , the spherical code can be expressed as $K(L, M_c, \theta)$, where $\theta \in (0, \pi]$ represents the angle between two point vectors. According to the Law of Cosines, the minimum Euclidean distance between two points of K is $d_{\min} = \sqrt{2 - 2\cos\theta}$ when θ reaches the maximum attainable value. Sloane, Hardin, and Smith have given the arrangements in three, four, and five dimensions with $M_c = 4, 5, \dots, 130$ [27]. For the four-dimensional spherical code, we choose $L = 4, M_c = 16$, and

$\theta = 67.19^\circ$, which maximizes the minimum distance $d_{\min} = 1.1066$ between constellation points [27]. Among the 16 points generated by spherical code $K(4, 16, 67.19^\circ)$, each constellation is a four-dimensional vector representing four information bits and is listed as a column of the constellation matrix $C'_{4,16}$:

$$C'_{4,16} = \begin{bmatrix} 0.2719 & -0.9228 & -0.2660 & -0.0610 \\ 0.1438 & -0.3165 & 0.0030 & -0.9376 \\ 0.1566 & -0.5843 & 0.7734 & -0.1897 \\ -0.2404 & -0.2245 & -0.9414 & 0.0747 \\ 0.7397 & -0.3101 & 0.2502 & 0.5423 \\ 0.7252 & -0.0080 & -0.6189 & -0.3015 \\ 0.2421 & 0.6419 & 0.5150 & 0.5139 \\ -0.6990 & 0.4390 & -0.3000 & 0.4781 \\ 0.7625 & 0.2618 & 0.4506 & -0.3834 \\ -0.2276 & -0.4922 & -0.1710 & 0.8226 \\ -0.3001 & 0.3434 & 0.6808 & -0.5732 \\ -0.6143 & 0.3162 & -0.3791 & -0.6156 \\ 0.2293 & 0.9096 & -0.2554 & -0.2340 \\ 0.3613 & 0.3580 & -0.5359 & 0.6739 \\ -0.5966 & -0.0533 & 0.6839 & 0.4165 \\ -0.7727 & -0.6169 & -0.0775 & -0.1278 \end{bmatrix}^T$$

Because the four-dimensional constellation point $\mathbf{c}_i = (c_{i,1}, c_{i,2}, c_{i,3}, c_{i,4})$ of \mathcal{A} is a four-dimensional vector, two two-dimensional symbols will be used jointly to carry a four-dimensional symbol in the OTFS-IM4 system. \mathbf{c}_i is transmitted by two-dimensional symbols $s_1 = c_{i,1} + jc_{i,2}$ and $s_2 = c_{i,3} + jc_{i,4}$. These two symbols are denoted as \mathbf{s}_β . Therefore, the number of active symbols k should be a multiple of 2, which means there are $k/2$ four-dimensional symbols in a sub-block. Consequently, the number of constellation mapping bits is $p_2 = k/2 \log_2(M_c)$.

To facilitate signal detection, we consider k as continuous, and non-overlap symbols are selected together as the active symbols among n symbols in a sub-block. The index set can then be represented as $\mathbf{I} = \{k(j-1) + 1, k(j-1) + 2, \dots, k(j-1) + k\}$, where j comes from the set $\{1, 2, \dots, n/k\}$ and is an integer in general. For example, the index selection lookup table when $n = 8, k = 2$ is depicted in Table 1. For the β -th sub-block, the index selection is a subset of the index set \mathbf{I} , denoted as \mathbf{I}_β . The number of index selection bits is $p_1 = \lfloor \log_2(n/k) \rfloor$. So far, the total bits in a sub-block are as follows:

$$p = p_1 + p_2 = \left\lfloor \log_2\left(\frac{n}{k}\right) \right\rfloor + \frac{k}{2} \log_2(M_c) \tag{2}$$

so the spectral efficiency is $SE = p/n$. Finally, the symbols of the β -th sub-block can be written as:

$$\mathbf{X}_\beta = \{x(1), x(2), \dots, x(n)\}, x(i) = \begin{cases} \mathbf{s}_\beta, & i \in \mathbf{I}_\beta \\ 0, & i \notin \mathbf{I}_\beta \end{cases} \tag{3}$$

Table 1. Lookup table for $n = 8$ and $k = 2$.

Bits	Indices	Sub-Blocks
00	[1 2]	$[s_1, s_2, 0, 0, 0, 0, 0, 0]$
01	[3 4]	$[0, 0, s_1, s_2, 0, 0, 0, 0]$
10	[5 6]	$[0, 0, 0, 0, s_1, s_2, 0, 0]$
11	[7 8]	$[0, 0, 0, 0, 0, 0, s_1, s_2]$

For the subsequent OTFS modulation, the modulated sub-blocks are organized into the OTFS frame \mathbf{X}_{DD} along the Doppler axis through the frame creator. The signal in the

TF domain is obtained from \mathbf{X}_{DD} via Inverse Symplectic Fast Fourier Transform (ISSFT). Then, it is converted to the time domain expressed as \mathbf{S} by Heisenberg transform and shaping pulse:

$$\mathbf{S} = \mathbf{G}_{tx} \mathbf{F}_M^H (\mathbf{F}_M \mathbf{X}_{DD} \mathbf{F}_N^H) = \mathbf{G}_{tx} \mathbf{X}_{DD} \mathbf{F}_N^H \tag{4}$$

where $\mathbf{G}_{tx}, \mathbf{F}_{num}, (\cdot)^H$ are the transmitted shaping pulse matrix, *num*-point normalized Fourier transform matrix, and Hermitian transformation, respectively. Thus, the transmitted signal \mathbf{s} in the time domain can be expressed as:

$$\mathbf{s} = \text{vec}(\mathbf{S}) = (\mathbf{F}_N^H \otimes \mathbf{G}_{tx}) \mathbf{x} \tag{5}$$

where $\text{vec}(\cdot)$ is the column-wise operation, \otimes is the Kronecker product, and \mathbf{x} is the column-wise vector of \mathbf{X}_{DD} .

The signal \mathbf{s} is transmitted over the time-varying channel, and then the received signal \mathbf{r} can be expressed as:

$$\mathbf{r} = \mathbf{H} \mathbf{s} + \mathbf{n} \tag{6}$$

where $\mathbf{n} \in \mathbb{C}^{MN \times 1}$ is the additive Gaussian white noise with mean 0 and variance N_0 , and $\mathbf{H} \in \mathbb{C}^{MN \times MN}$ is the channel matrix in the time domain. The expression of \mathbf{H} is as follows:

$$\mathbf{H} = \sum_{i=1}^P h_i \mathbf{\Pi}^i \mathbf{\Delta}^{(k_i)} \tag{7}$$

where P is the number of propagation paths, h_i is the channel gain of the i -th path, $\mathbf{\Pi} = \text{circ}([0, 1, \dots, 0]_{MN \times 1}^T) \in \mathbb{C}^{MN \times MN}$ is the permutation matrix (forward cyclic shift) reflecting the delay, and $\mathbf{\Delta} = \text{diag}\{e^{j2\pi(0)/MN}, e^{j2\pi(1)/MN}, \dots, e^{j2\pi(MN-1)/MN}\} \in \mathbb{C}^{MN \times MN}$ is the diagonal matrix reflecting the Doppler.

The received signal \mathbf{r} can also be rewritten as an $M \times N$ matrix \mathbf{R} by the inverse column-wise operation. In order to obtain the received signal \mathbf{y} in the DD domain, the receiver performs in reverse compared with the transmitter, including in its shaping pulse, Wigner transform, Symplectic Fast Fourier Transform (SSFT), and column-wise operation:

$$\mathbf{Y}_{DD} = \mathbf{F}_M^H (\mathbf{F}_M \mathbf{G}_{rx} \mathbf{R}) \mathbf{F}_N = \mathbf{G}_{rx} \mathbf{R} \mathbf{F}_N \tag{8}$$

$$\mathbf{y} = \text{vec}(\mathbf{Y}_{DD}) = (\mathbf{F}_N \otimes \mathbf{G}_{rx}) \mathbf{r} \tag{9}$$

where $\mathbf{Y}_{DD}, \mathbf{G}_{rx}$ represent the matrix form of the received signal in DD domain and the received shaping pulse matrix, respectively.

Combined with Equations (5), (6) and (9), the input–output relationship in the DD domain can be expressed as:

$$\begin{aligned} \mathbf{y} &= (\mathbf{F}_N \otimes \mathbf{G}_{rx}) \mathbf{H} (\mathbf{F}_N^H \otimes \mathbf{G}_{tx}) \mathbf{x} + (\mathbf{F}_N \otimes \mathbf{G}_{rx}) \mathbf{n} \\ &= \mathbf{H}_{eff} \mathbf{x} + \tilde{\mathbf{n}} \end{aligned} \tag{10}$$

where $\mathbf{H}_{eff} = \sum_{i=1}^P h_i [(\mathbf{F}_N \otimes \mathbf{G}_{rx}) \mathbf{\Pi}^i \mathbf{\Delta}^{(k_i)} (\mathbf{F}_N^H \otimes \mathbf{G}_{tx})]$.

It is assumed that the channel state information is well known at the receiver. After the MMSE equalization for \mathbf{Y}_{DD} , the estimated signal $\hat{\mathbf{X}}_{DD}$ in the DD domain is obtained. The MMSE equalization used in this paper is a basic MMSE approach that can be expressed as follows [9]:

$$\hat{\mathbf{x}}_{DD} = \mathbf{H}_{eff}^H (\mathbf{H}_{eff} \mathbf{H}_{eff}^H + \frac{1}{N_{0,DD}} \mathbf{I})^{-1} \mathbf{Y}_{DD} \tag{11}$$

where $\hat{\mathbf{x}}_{DD}$ is the column-wise vector of $\hat{\mathbf{X}}_{DD}$, \mathbf{y}_{DD} is the column-wise vector of \mathbf{Y}_{DD} , and $N_{0,DD} = N_0$ represents the variance in noise in the DD domain. The noise vectors in the time domain and the DD domain have the same statistical properties since they are related

by unitary transformations. Then, the ML detector is used to demodulate the signals, sub-block by sub-block. The index information and the modulated symbols information in the β -th sub-block are detected as:

$$[\mathbf{I}_\beta, \mathbf{s}_\beta] = \arg \min_{\mathbf{I}_\beta, \mathbf{s}_\beta} \left| \hat{\mathbf{X}}_\beta - \mathbf{X}_\beta \right|^2 \tag{12}$$

where \mathbf{X}_β is the potential cases of sub-blocks. For each sub-block, there are $(M_c)^{k/2}$ possible options for the modulated symbols, and there are n/k different situations for index selection. Therefore, the number of potential cases for a sub-block is $O((M_c)^{k/2}n/k)$, which is also the complexity of detecting a sub-block using the ML detection algorithm.

3. Performance Analysis

In this section, we analyze the performance of the OTFS-IM4 system by deriving the approximation value of the BER and the upper bound of the PAPR.

3.1. BER

When CSI is well known at the receiver, it can be seen from Equation (6) that the conditional pairwise error probability (CPEP) of misjudging \mathbf{x} as $\hat{\mathbf{x}}$ is as follows [28]:

$$\Pr(\mathbf{x} \rightarrow \hat{\mathbf{x}} | \mathbf{H}_{eff}) = Q\left(\sqrt{\frac{\|\mathbf{H}_{eff}(\hat{\mathbf{x}} - \mathbf{x})\|^2}{2N_{0,DD}}}\right) \tag{13}$$

where $Q(\cdot)$ is the Gaussian Q function. In order to obtain the non-conditional probability, it is necessary to calculate the expected \mathbf{H}_{eff} . To facilitate the solution, the input–output expression is rewritten into a form related to the channel gain \mathbf{h} :

$$\mathbf{y} = \Phi(\mathbf{x})\mathbf{h} + \tilde{\mathbf{n}} \tag{14}$$

where $\Phi(\mathbf{x}) = [\Phi_1\mathbf{x}, \Phi_2\mathbf{x}, \dots, \Phi_P\mathbf{x}] \in \mathbb{C}^{MN \times P}$, $\Phi_i = (\mathbf{F}_N \otimes \mathbf{G}_{rx}) \mathbf{\Pi}^i \Delta^{(k_i)} (\mathbf{F}_N^H \otimes \mathbf{G}_{tx}) \in \mathbb{C}^{MN \times MN}$, $\mathbf{h} = [h_1, h_2, \dots, h_P]^T \in \mathbb{C}^{P \times 1}$, and $h_i \sim CN(0, \sigma^2)$. The CPEP can be expressed as:

$$\Pr(\mathbf{x} \rightarrow \hat{\mathbf{x}} | \mathbf{h}) = Q\left(\sqrt{\frac{\|(\Phi(\hat{\mathbf{x}}) - \Phi(\mathbf{x}))\mathbf{h}\|^2}{2N_{0,DD}}}\right) = Q\left(\sqrt{\frac{\alpha}{2N_{0,DD}}}\right) \tag{15}$$

where $\alpha = \mathbf{h}^H ((\Phi(\hat{\mathbf{x}}) - \Phi(\mathbf{x}))^H ((\Phi(\hat{\mathbf{x}}) - \Phi(\mathbf{x}))\mathbf{h}) = \mathbf{h}^H \Theta \mathbf{h}$. Then, substitute the approximation of the Q function into (15):

$$\Pr(\mathbf{x} \rightarrow \hat{\mathbf{x}} | \mathbf{h}) \approx \frac{1}{12} e^{-\frac{\alpha}{4N_{0,DD}}} + \frac{1}{4} e^{-\frac{\alpha}{3N_{0,DD}}} \tag{16}$$

The unconditional pairwise error probability (UPEP) is calculated as follows [28]:

$$\begin{aligned} \Pr(\mathbf{x} \rightarrow \hat{\mathbf{x}}) &= E_{\mathbf{h}}(\Pr(\mathbf{x} \rightarrow \hat{\mathbf{x}} | \mathbf{h})) \\ &= \frac{1/12}{\det(\mathbf{I}_P + \frac{1}{4N_{0,DD}} \mathbf{K}_P \Theta)} + \frac{1/4}{\det(\mathbf{I}_P + \frac{1}{3N_{0,DD}} \mathbf{K}_P \Theta)} \end{aligned} \tag{17}$$

where $\mathbf{K}_P = E(\mathbf{h}\mathbf{h}^H) = \sigma^2 \mathbf{I}_P$. It is obvious that Θ is the Hermitian matrix and can be decomposed into $\Theta = \mathbf{U}\mathbf{\Lambda}\mathbf{U}^H$, where $\mathbf{\Lambda} = \text{diag}(\lambda_1, \lambda_2, \dots, \lambda_P)$, and λ_i is the eigenvalue of Θ . Hence, $\det(\Theta) = \prod_{i=1}^P \lambda_i$, and we can simplify (17) as:

$$\Pr(\mathbf{x} \rightarrow \hat{\mathbf{x}}) = \frac{1/12}{\prod_{i=1}^P (1 + \frac{\sigma^2}{4N_{0,DD}} \lambda_i)} + \frac{1/4}{\prod_{i=1}^P (1 + \frac{\sigma^2}{3N_{0,DD}} \lambda_i)} \tag{18}$$

Finally, the BER can be expressed as:

$$P_b = \frac{1}{pgn_x} \sum_{\mathbf{x}} \sum_{\hat{\mathbf{x}} \neq \mathbf{x}} \Pr(\mathbf{x} \rightarrow \hat{\mathbf{x}}) e(\mathbf{x}, \hat{\mathbf{x}}) \tag{19}$$

where $n_x = ((M_c)^{k/2} n/k)^\delta$ is the number of potential cases of signal \mathbf{x} , and $e(\mathbf{x}, \hat{\mathbf{x}})$ denotes the number of error bits when \mathbf{x} is detected as $\hat{\mathbf{x}}$. Additionally, the error bits from misjudging includes the modulation symbol only, the index selection only, and both.

3.2. PAPR

The transmitted signal \mathbf{s} can be also represented as $s[u, v], 0 \leq u \leq M - 1, 0 \leq v \leq N - 1$ [29]:

$$s(u + vM) = M \sum_{n=0}^{N-1} \tilde{x}_u[n] g_{tx}([u + vM - nM]_{MN}) \tag{20}$$

where $\tilde{x}_u[n] = \sum_{k=0}^{N-1} x[k, u] e^{j2\pi \frac{nk}{N}}$ is the N -point IFFT of the DD domain signal $x[k, u]$ along the Doppler axis. According to the system model, \mathbf{X}_{DD} contains N/n sub-blocks in each row. Therefore, there are kN/n active symbols from \mathcal{A} or zero otherwise in each row of \mathbf{X}_{DD} . For the u -th row of \mathbf{X}_{DD} , we denote $E\{|x[k, u]|_2\} = \sigma_x^2$ and $E\{|\tilde{x}_u[n]|_2\} = N\sigma_x^2$.

The maximum peak-to-average-power ratio (PAPR) of the transmitted signal \mathbf{s} is:

$$\text{PAPR} = \frac{\max_{u,v} \{|s(u + vM)|_2\}}{P_{avg}} \tag{21}$$

where P_{avg} is the average energy of \mathbf{s} and can be expressed as:

$$\begin{aligned} P_{avg} &= \frac{1}{MN} \sum_{v=0}^{N-1} \sum_{u=0}^{M-1} E\{|s(u + vM)|_2\} \\ &= M\sigma_x^2 \sum_{v=0}^{N-1} \sum_{u=0}^{M-1} \sum_{n=0}^{N-1} E\{|g_{tx}([u + vM - nM]_{MN})|_2\} \end{aligned} \tag{22}$$

The numerator of Equation (20) is simplified by the Cauchy–Schwartz inequality:

$$\begin{aligned} \max_{u,v} \{|s(u + vM)|_2\} &\leq M^2 \max_u \sum_{n=0}^{N-1} |\tilde{x}_u[n]|^2 \\ &\max_{u,v} \sum_{n=0}^{N-1} |g_{tx}([u + vM - nM]_{MN})|^2 \end{aligned} \tag{23}$$

For a certain u , according to discrete Parseval’s theorem, we have:

$$\begin{aligned} \max_u \sum_{n=0}^{N-1} |\tilde{x}_u[n]|^2 &= N \max_u \sum_{k=0}^{N-1} |x[k, u]|^2 \\ &\leq \frac{k}{n} N^2 \max_{k,l} |x[k, l]|^2 \end{aligned} \tag{24}$$

Therefore, Equation (23) is simplified as follows:

$$\begin{aligned} \max_{u,v} \{|s(u + vM)|_2\} &\leq M^2 N^2 \frac{k}{n} \max_{k,l} |x[k, l]|_2 \\ &\max_{u,v} \sum_{n=0}^{N-1} |g_{tx}([u + vM - nM]_{MN})|^2 \end{aligned} \tag{25}$$

For the rectangular pulse shaping function, the upper bound of PAPR is:

$$\text{PAPR} \leq \frac{\frac{kN}{n} \max_{k,l} |x[k, l]|^2}{\sigma_x^2} \quad (26)$$

The PAPR of the OTFS-IM system increases linearly with the number of active symbols in each row of \mathbf{X}_{DD} rather than N , which indicates that the PAPR of the OTFS-IM system is lower than that of the OTFS system. Under the same sub-block parameters, a four-dimensional symbol is carried by two two-dimensional symbols. These two two-dimensional symbols are not of uniform amplitude, but they are uniform in two-dimensional modulation. Therefore, the PAPR of four-dimensional modulation is slightly different from that of the two-dimensional modulation, which we will verify by simulation in Section 4.

4. Simulation Results

In Sections 2 and 3, the general model of the proposed system and the mathematical expression of performance have been discussed in detail. Then, in this section, we simulate and examine the reliability and robustness of the proposed scheme and compare it with the conventional OTFS-IM scheme [18]. Additionally, the simulation results and mathematical analysis are also compared to verify the correctness of the derivation.

As mentioned before, we focus on the four-dimensional spherical code $K(4, 16, 67.19^\circ)$, whose constellation matrix $C'_{4,16}$ is normalized, and two two-dimensional symbols convey one four-dimensional symbol, meaning that the total energy of a sub-block is $k/2$. However, in the traditional OTFS-IM system, the total energy of k active symbols in a sub-block is k . In order to maintain the same energy, the actual amplitude of each constellation point of \mathcal{A} should be $\sqrt{2}$, which changes the constellation matrix as $C_{4,16} = \sqrt{2}C'_{4,16}$ and the minimum distance as $d_{\min} = \sqrt{2} \times 1.1066$. An example of the index selection relationship is illustrated in Table 1, where a sub-block transmits a four-dimensional constellation point with the total bits $p = 6$. Therefore, the bit signal-to-noise ratio is $E_b/N_0 = k/(pN_0)$. Furthermore, we consider an OTFS frame with $M = 64$ and $N = 8$. The operating carrier frequency is $f_c = 3$ GHz, and the subcarrier spacing is $\Delta f = 15$ kHz. As the number of paths in A2G communication is generally small, we model the channel as a two-path model, with reference to the model of the NTN-TDL series of the 3GPP standard [30]. The maximum speed of the UAV is set to 500 km/h, and the maximum delay is about 4 μ s.

In Figure 2, we compare the BER performance of our proposed OTFS-IM4 scheme with that of the traditional OTFS-IM2 scheme. According to reference [17], the number of transmitted bits in a sub-block of the OTFS-IM2 system is $p = \log_2(C_n^k) + k \log_2(M_c)$. For fairness, sub-block parameters $n = 4, k = 1$ and BPSK modulation are selected in the traditional two-dimensional modulation to transmit the same number of bits as the four-dimensional modulation. At this time, the lookup table in the OTFS-IM2 system has only four options to choose, which is the same as in the proposed scheme, and the spectral efficiencies are all $\text{SE} = 3/4$. As discussed in Section 2, MMSE equalization and ML detection are performed successively for signal detection. It is obvious that the four-dimensional modulation has almost 2 dB gain compared with the two-dimensional modulation, which is consistent with the classic detection theory. Thus, the bit signal-to-noise ratio can be reduced under the acceptable BER, which plays an important role in saving the transmitting power and prolonging the flight time of the UAV. Since MMSE equalization needs to calculate the matrix inverse, the complexity is $O(M^3N^3)$, which exponentially increases as the OTFS frame size grows. In contrast, the complexity of the MRC algorithm is $O(MN|L|n_{\text{iter}})$ [15], where $|L|$ represents the number of distinct delay paths among P propagation paths, and $n_{\text{iter}} < 20$ denotes the number of iterations for the MRC algorithm. Therefore, the complexity of the MRC algorithm is lower than that of the MMSE algorithm. In addition, it can easily be used in the index modulation system for equalization by converting hard decisions into soft decisions. It can be seen that the

performance of MRC is gradually better than MMSE when the E_b/N_0 exceeds 10 dB. In particular, MRC equalization performs better than MMSE equalization, with more than 2 dB gain when the BER is 10^{-4} . However, there is zero padding in MRC equalization, which leads to a decrease in spectral efficiency [15]. In summary, there is a trade-off between application and performance. Therefore, an appropriate equalization method should be selected based on application scenarios in reality.

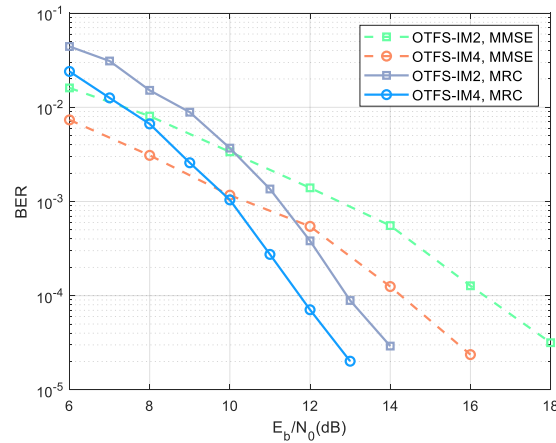


Figure 2. BER performance comparison between OTFS-IM4 and OTFS-IM2 in the two-path channel.

Figure 3 presents the generalization of the OTFS-IM4 system at different speeds. To thoroughly investigate the effects of different Dopplers, we have taken into account both small UAV scenarios and higher-speed scenarios, such as those with military UAVs and future aircraft. Therefore, the selected flight speeds in simulation are 100 km/h and 500 km/h. As the speed increases, the BER performance behaves similarly, except there is a slight difference that proves the effectiveness of the OTFS-IM4 at different moving speeds. This means that under the same BER threshold and energy consumption, when transmitting signals are in the same communication range, a UAV in the OTFS-IM4 system can have a higher moving speed or have a larger communication range at the same speed.

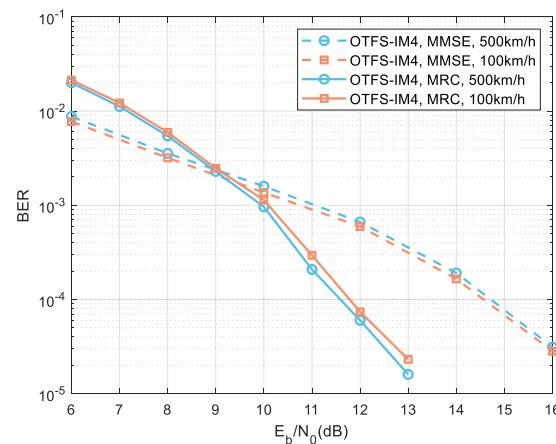


Figure 3. BER performance for different speeds in two propagation paths.

Figure 4 simulates the performance of an OTFS-IM system with a six-dimensional spherical code (denoted as OTFS-IM6) to analyze the robustness of the proposed system. According to the system model in Section 2, when the 64-point spherical code is used for six-dimensional modulation, the sub-block parameters are selected as $n = 6$ and $k = 3$. Since sub-blocks are organized along the Doppler axis, we choose the OTFS frame with $M = 64$ and $N = 12$ to ensure that the sub-block will not be separated. Other parameters remain the same as in Figure 2. As can be seen from Figure 4, the performance of MMSE

equalization is about 4.5 dB lower than that of MRC when $\text{BER} = 10^{-4}$. Additionally, in the MRC equalization results, the six-dimensional modulation has a gain of more than 1.5 dB compared with the two-dimensional modulation. It is 0.5 dB higher than the gain between the OTFS-IM4 system and the OTFS-IM2 system in Figure 2. The conclusion drawn is that the higher the dimension, the better the performance. However, the detection is sub-block by sub-block in the proposed scheme using the ML method. The complexity of detecting a sub-block is $O((M_c)^{k/3} n/k)$ in the six-dimensional modulation and then the complexity of detecting an OTFS frame will be $O(((M_c)^{k/3} n/k)^S)$. Therefore, the higher the dimension and the higher the number of constellation points, the higher the complexity. In this paper, four-dimensional modulation is chosen to take into account both performance and detection complexity.

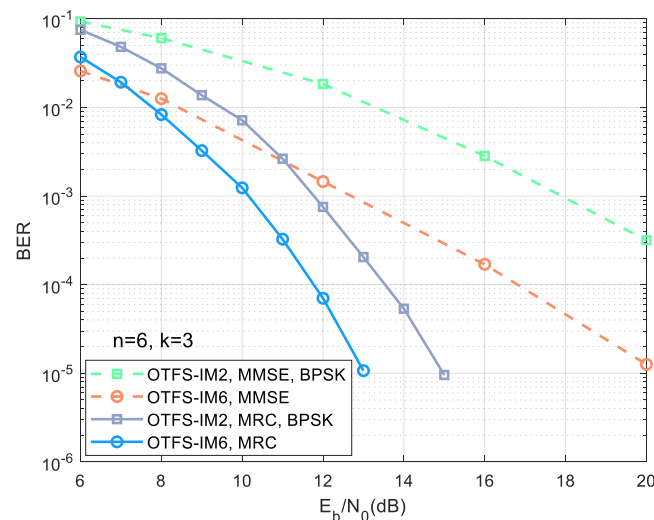


Figure 4. BER performance comparison between OTFS-IM6 and OTFS-IM2 in the two-path channel.

Additionally, we also simulate the BER performance of these two schemes in the EVA channel to verify the generality of the proposed scheme while the other parameters are the same as the two-path channel. It can be seen in Figure 5a that the four-dimensional modulation is still better than the two-dimensional modulation. For example, the OTFS-IM4 scheme achieves about 1.5 dB gain more than the OTFS-IM2 scheme when $\text{BER} = 10^{-4}$. Moreover, when QPSK is adopted in the two-dimensional modulation, the spectral efficiency is $\text{SE} = 1$, and the BER performance coincides with BPSK, which is the same conclusion as in the AWGN channel. Figure 5b demonstrates a comparison between the proposed scheme and BPSK and QPSK under the EVA channel, considering an increased number of symbols within an OTFS frame. The only difference from the conditions in Figure 5a is that the size of an OTFS frame is changed to $M = 64$, $N = 16$. At this time, the number of symbols in a frame is $MN/n * k = 64 * 16/8 * 2 = 256$. The same conclusion is reached as shown in Figure 5a. Due to the Doppler resolution $\Delta\nu = 1/NT$, the Doppler resolution improves when N increases. Therefore, the BER performance also improves accordingly, which explains the difference between the two figures. Results show that the proposed scheme is also applicable when the channel is more complex, which verifies the robustness and generality of the OTFS-IM scheme with four-dimensional spherical code.

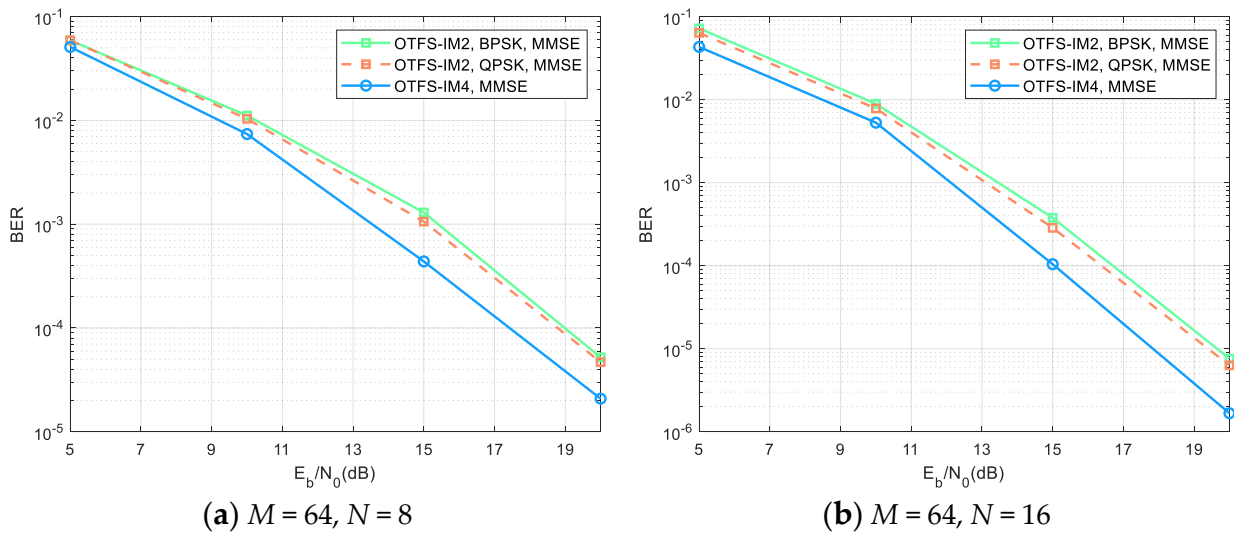


Figure 5. BER performance comparison between OTFS-IM4 and OTFS-IM2 in the EVA channel.

The comparison of theoretical values and simulation results for BER and PAPR performance in the OTFS-IM4 system are well illustrated in the following. First, the BER comparison is shown in Figure 6. Since the derived BER theoretical value needs to traverse the entire signal space, the calculation complexity of the theoretical value is relatively high. In order to facilitate the solution, the simulation parameters are specified as follows. The OTFS frames are simplified to $M = 4$ and $N = 2$. Since the symbol duration T and the sub-carrier spacing Δf determine the maximum delay τ_{\max} and maximum Doppler ν_{\max} that can be supported for the channel [31], we adapt the channel state to $[l_i, k_i] = \{[0, 0], [1, 1]\}$ and $h_i \sim CN(0, 1/P)$. Other parameters are the same as in the four-dimensional modulation. There is exactly one sub-block in a frame in this case, i.e., $g = 1, p = 6$, and $n_x = 64$. It can be seen that the simulation results and the theoretical values become closer as E_b/N_0 increases, which verifies the correctness of the derived BER performance.

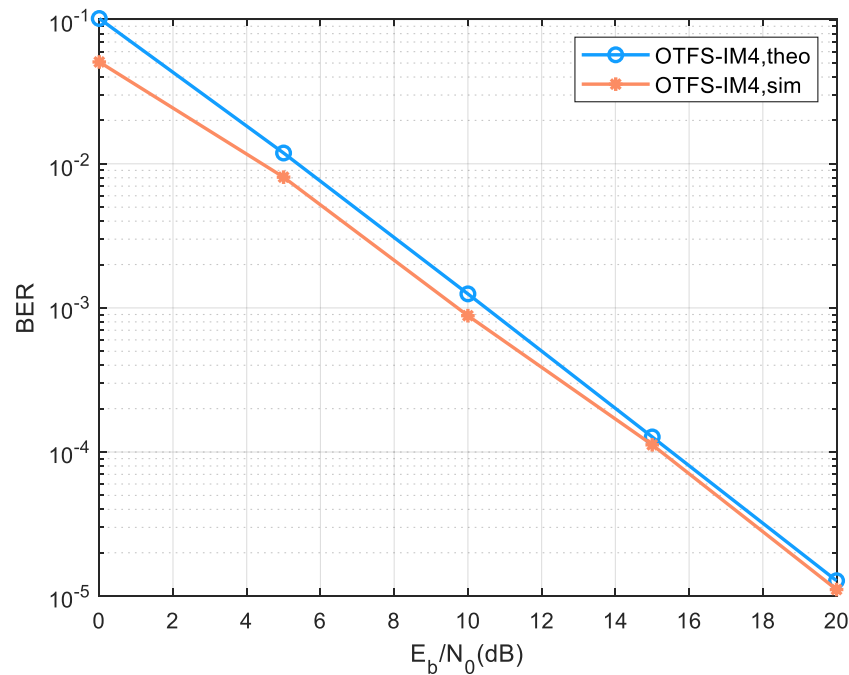


Figure 6. BER comparison of theoretical values and simulation results in the OTFS-IM4 system.

Next, Figure 7 simulates the CCDF of the PAPR for different OTFS schemes and different sub-block situations. The theoretical analysis results show that PAPR in the OTFS system is related to the parameter N , while in the OTFS-IM system, PAPR is also related to the proportion of the active symbols in the sub-block. Therefore, different N values are simulated to verify the analysis results. We take $N = 16$ and $N = 32$ for an example. Meanwhile, BPSK modulation is still used in the OTFS-IM2 system. When $N = 16$, the simulation results are as shown in Figure 7a, and there is the following specific analysis. The spectral efficiency of the two solid curves is $SE = 3/4$. It can be seen that the PAPR performance of the OTFS-IM2 is similar to that of the OTFS-IM4. When the spectral efficiency is $SE \approx 1$, as shown by the two dashed lines, the PAPR performance of the OTFS-IM4 is about 0.1 dB better than that of the OTFS-IM2. As for the theoretical analysis in Section 3, the PAPR performance of these two schemes is only slightly different. In addition, it is proved that the PAPR increases linearly with the proportion k/n of active symbols in a sub-block. Theoretically, the PAPR with $k/n = 1/4$ is 3 dB smaller than with $k/n = 1/2$, which corresponds to the simulation results. For $N = 32$, the simulation results are depicted in Figure 7b. Although there are slight differences in performance compared with that in Figure 7a, the trend is the same. When $CCDF = 10^{-3}$, the PAPR with $SE = 3/4$ is approximately equal in OTFS-IM2 and OTFS-IM4, and the four-dimensional modulation has 0.1 dB gain over two-dimensional modulation at $SE \approx 1$. Comparing Figure 7a,b horizontally, PAPR increases by 3 dB with the doubling of N when spectral efficiency is the same, which is also consistent with the theoretical analysis. Additionally, the PAPR of the OTFS system is proportional to N but has a threshold.

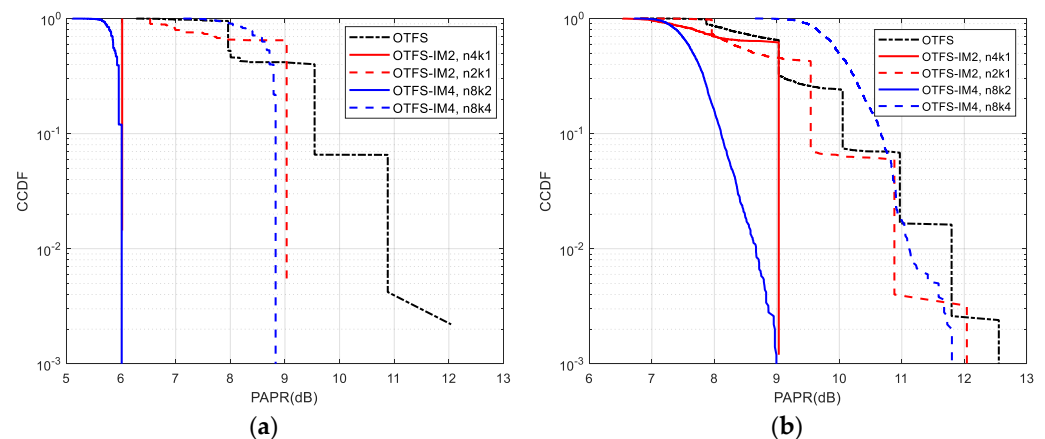


Figure 7. The CCDF comparison of different schemes: (a) $N = 16$, (b) $N = 32$.

5. Conclusions

In this paper, we investigated the OTFS-IM system based on the four-dimensional spherical code to enhance the performance by utilizing the advantage of the increased distance between constellation points in higher dimensions. On the one hand, achieving the requirement of BER at a lower signal-to-noise ratio is conducive to reducing power consumption and improving the endurance of UAVs in A2G communication. On the other hand, the scheme proposed in this paper to improve the performance is more concise and convenient; it does not increase the number of steps of the transmitter in the same way as most existing studies, i.e., by increasing the index dimension. Moreover, we analyzed the performance of a practical OTFS-IM4 system, which includes the analysis of the approximate value of the BER and the upper bound of the PAPR. It is worth noting that there is a trade-off between spectral efficiency and PAPR due to the different activation proportions in the sub-blocks. The simulation results demonstrate that our proposed OTFS-IM4 system is capable of providing more than 1 dB performance gain over the traditional OTFS-IM with two-dimensional modulation. It is proved that the proposed system has stronger robustness and generality. Furthermore, our theoretical derivations

for OTFS-IM4 are also verified by simulation results, which theoretically supports the proposed system's performance. It is also worth noting that, in the future, research can be conducted to further explore four-dimensional spherical code and better-performing equalization techniques, such as an iterative MMSE method [32].

Author Contributions: Conceptualization, J.Z.; methodology, L.G.; software, P.G.; validation, G.L., S.J. and J.Z.; formal analysis, L.G.; investigation, P.G.; writing—original draft preparation, P.G.; writing—review and editing, L.G.; supervision, G.L. and J.Z. All authors have read and agreed to the published version of the manuscript.

Funding: This work was supported by the technology project of State Grid (5700-202214478A-2-0-KJ).

Data Availability Statement: Not applicable.

Acknowledgments: The authors would like to thank the editor and the anonymous referees for their instructive comments.

Conflicts of Interest: The authors declare no conflict of interest.

References

- Zhang, C.; Zhang, L.; Zhu, L.; Zhang, T.; Xiao, Z.; Xia, X.G. 3D Deployment of Multiple UAV-Mounted Base Stations for UAV Communications. *IEEE Trans. Commun.* **2021**, *69*, 2473–2488. [\[CrossRef\]](#)
- Wang, C.-N.; Yang, F.-C.; Vo, N.T.M.; Nguyen, V.T.T. Wireless Communications for Data Security: Efficiency Assessment of Cybersecurity Industry—A Promising Application for UAVs. *Drones* **2022**, *6*, 363. [\[CrossRef\]](#)
- Zeng, Y.; Lyu, J.; Zhang, R. Cellular-connected UAV: Potential, challenges, and promising technologies. *IEEE Wirel. Commun.* **2018**, *26*, 120–127. [\[CrossRef\]](#)
- Zhang, L.; Wang, Z.; Zheng, G. OF-FSE: An Efficient Adaptive Equalization for QAM-Based UAV Modulation Systems. *Drones* **2023**, *7*, 525. [\[CrossRef\]](#)
- Bing, L.; Hu, L.; Gu, Y.; Yin, Y. Drone-Aided Networking with Massive Connectivity and High Spectral Efficiency Enabled. *Drones* **2023**, *7*, 363. [\[CrossRef\]](#)
- Pawase, C.J.; Chang, K. 5G-NR Physical Layer-Based Solutions to Support High Mobility in 6G Non-Terrestrial Networks. *Drones* **2023**, *7*, 176. [\[CrossRef\]](#)
- Bai, L.; Han, R.; Liu, J.; Yu, Q.; Choi, J.; Zhang, W. Air-to-Ground Wireless Links for High-Speed UAVs. *IEEE J. Sel. Areas Commun.* **2020**, *38*, 2918–2930. [\[CrossRef\]](#)
- Mao, B.; Tang, F.; Kawamoto, Y.; Kato, N. Optimizing Computation Offloading in Satellite-UAV-Served 6G IoT: A Deep Learning Approach. *IEEE Netw.* **2021**, *35*, 102–108. [\[CrossRef\]](#)
- Linsalata, F.; Albanese, A.; Sciancalepore, V.; Roveda, F.; Magarini, M.; Costa-Perez, X. OTFS-superimposed PRACH-aided Localization for UAV Safety Applications. In Proceedings of the IEEE Global Communications Conference (GLOBECOM), Madrid, Spain, 7–11 December 2021.
- Hadani, R.; Rakib, S.; Tsatsanis, M.; Monk, A.; Goldsmith, A.J.; Molisch, A.F.; Calderbank, R. Orthogonal Time Frequency Space Modulation. In Proceedings of the IEEE Wireless Communications and Networking Conference (WCNC), San Francisco, CA, USA, 19–22 March 2017.
- Raviteja, P.; Phan, K.T.; Jin, Q.; Hong, Y.; Viterbo, E. Low-Complexity Iterative Detection for Orthogonal Time Frequency Space Modulation. In Proceedings of the IEEE Wireless Communications and Networking Conference (WCNC), Barcelona, Spain, 15–18 April 2018.
- Liang, Y.; Li, L.; Fan, P.; Guan, Y. Doppler Resilient Orthogonal Time-Frequency Space (OTFS) Systems Based on Index Modulation. In Proceedings of the 2020 IEEE 91st Vehicular Technology Conference (VTC2020-Spring), Antwerp, Belgium, 25–28 May 2020; pp. 1–5.
- Tiwari, S.; Das, S.S.; Rangamgari, V. Low complexity LMMSE Receiver for OTFS. *IEEE Commun. Lett.* **2019**, *23*, 2205–2209. [\[CrossRef\]](#)
- Raviteja, P.; Phan, K.T.; Hong, Y.; Viterbo, E. Interference Cancellation and Iterative Detection for Orthogonal Time Frequency Space Modulation. *IEEE Trans. Wirel. Commun.* **2018**, *17*, 6501–6515. [\[CrossRef\]](#)
- Thaj, T.; Viterbo, E. Low Complexity Iterative Rake Decision Feedback Equalizer for Zero-Padded OTFS Systems. *IEEE Trans. Veh. Technol.* **2020**, *69*, 15606–15622. [\[CrossRef\]](#)
- Yuan, W.; Wei, Z.; Yuan, J.; Ng, D.W.K. A Simple Variational Bayes Detector for Orthogonal Time Frequency Space (OTFS) Modulation. *IEEE Trans. Veh. Technol.* **2020**, *69*, 7976–7980. [\[CrossRef\]](#)
- Raviteja, P.; Phan, K.T.; Hong, Y. Embedded Pilot-Aided Channel Estimation for OTFS in Delay-Doppler Channels. *IEEE Trans. Veh. Technol.* **2019**, *68*, 4906–4917. [\[CrossRef\]](#)
- Wang, S.; Guo, J.; Wang, X.; Yuan, W.; Fei, Z. Pilot Design and Optimization for OTFS Modulation. *IEEE Wirel. Commun. Lett.* **2021**, *10*, 1742–1746. [\[CrossRef\]](#)

19. Wei, Z.; Yuan, W.; Li, S.; Yuan, J.; Ng, D.W.K. Off-Grid Channel Estimation with Sparse Bayesian Learning for OTFS Systems. *IEEE Trans. Wirel. Commun.* **2022**, *21*, 7407–7426. [[CrossRef](#)]
20. Guo, L.; Gu, P.; Zou, J.; Liu, G.; Shu, F. DNN-Based Fractional Doppler Channel Estimation for OTFS Modulation. *IEEE Trans. Veh. Technol.* **2023**. Early Access. [[CrossRef](#)]
21. Francis, J.K.; Augustine, R.M.; Chockalingam, A. Diversity and PAPR Enhancement in OTFS using Indexing. In Proceedings of the IEEE 93rd Vehicular Technology Conference (VTC-Spring), Electr Network, Helsinki, Finland, 25–28 April 2021.
22. Zhao, H.; He, D.; Kang, Z.; Wang, H. Orthogonal Time Frequency Space (OTFS) With Dual-Mode Index Modulation. *IEEE Wirel. Commun. Lett.* **2021**, *10*, 991–995. [[CrossRef](#)]
23. Feng, D.; Zheng, J.; Bai, B.; Jiang, J.; Zheng, L. In-Phase and Quadrature Index Modulation Aided OTFS Transmission. *IEEE Commun. Lett.* **2022**, *26*, 1318–1322. [[CrossRef](#)]
24. Han, R.; Ma, J.; Bai, L. Trajectory Planning for OTFS-Based UAV Communications. *China Commun.* **2023**, *20*, 114–124. [[CrossRef](#)]
25. Goldsmith, A. *Wireless Communications*; Cambridge University Press: Cambridge, UK, 2005.
26. Conway, J.H.; Sloane, N.J.A. *Sphere Packings, Lattices and Groups*; Springer: Berlin/Heidelberg, Germany, 1988.
27. Spherical Codes. Available online: <http://neilsloane.com/packings/index.html#I> (accessed on 23 January 2021).
28. Basar, E.; Aygolu, U.; Panayirci, E.; Poor, H.V. Orthogonal Frequency Division Multiplexing with Index Modulation. *IEEE Trans. Signal Process.* **2013**, *61*, 5536–5549. [[CrossRef](#)]
29. Naveen, C.; Sudha, V. Peak-to-Average Power Ratio reduction in OTFS modulation using companding technique. In Proceedings of the 5th International Conference on Devices, Circuits and Systems (ICDCS), Coimbatore, India, 5–6 March 2020; pp. 140–143.
30. 3GPP. *TR 38.811; Study on New Radio (NR) to Support Nonterrestrial Networks*. 3rd Generation Partnership Project (3GPP): Valbonne, France, 2020; pp. 90–92.
31. Hong, Y.; Thaj, T.; Viterbo, E. *Delay-Doppler Communications: Principles and Applications*; Academic Press: Cambridge, MA, USA, 2022.
32. Li, Q.; Yuan, J.; Lin, H. Iterative MMSE Detection for Orthogonal Time Frequency Space Modulation. In Proceedings of the 2022 IEEE International Conference on Communications Workshops (ICC Workshops), Seoul, Republic of Korea, 16–20 May 2022; pp. 1–6.

Disclaimer/Publisher’s Note: The statements, opinions and data contained in all publications are solely those of the individual author(s) and contributor(s) and not of MDPI and/or the editor(s). MDPI and/or the editor(s) disclaim responsibility for any injury to people or property resulting from any ideas, methods, instructions or products referred to in the content.